AIAA Journal
Vol. 45, No. 10, October 2007

Flow over NACA-0009 and Eppler-61 Airfoils at Reynolds Numbers 5000 to 60,000

Y. Elimelech,* R. Arieli,† and G. Iosilevskii‡
Technion–Israel Institute of Technology, 32000 Haifa, Israel

DOI: 10.2514/1.22376

The flow about NACA-0009 and Eppler-61 airfoils at (chord-based) Reynolds numbers between 5000 and 60,000 is studied using flow visualizations and incompressible, time-accurate, two-dimensional, laminar Navier–Stokes simulations. Good agreement is found between experimental and numerically simulated flow patterns, as long as the flow remained nonturbulent. The study outlines three phases of angle-of-attack-dependent transition from fully laminar to partly turbulent flow around the airfoils, which are universally applicable at these Reynolds numbers. The first phase is characterized by a laminar wake that appears stable for at least a few chords behind the airfoil; in the second phase, the wake reforms into a well-ordered vortex street; in the third phase, this street becomes unstable and a separation bubble is formed on the suction side of the airfoil. The pattern of the flow changes phases as the angle of attack increases; the exact angles at which the change occurs are airfoil- and Reynolds-number-dependent.

Nomenclature

C_f = friction coefficient, $2\tau_w/\rho u_\infty^2$
C_p = pressure coefficient, $2(p - p_\infty)/\rho u_\infty^2$
c = chord length
p = local pressure
p_∞ = pressure far from the wing
Re = Reynolds number (based on the chord length)
u_∞ = freestream velocity
ν = kinematic viscosity
ρ = density
τ_w = shear stress on the surface of the airfoil

I. Introduction

AERODYNAMIC characteristics of an airfoil change with the Reynolds number [1–3]. At Reynolds numbers of a few million (based on the chord length), the flow over the suction side of a conventional airfoil has no peculiarities. Typically, it is attached at small angles of attack (AOA), partly detached in the vicinity of the trailing edge at higher angles of attack, and fully detached at yet higher angles [4]. This pattern is associated with the bucketlike dependence of the drag coefficient on the angle of attack [3] and imperceptible dependence of the drag and maximal lift coefficients on the freestream turbulence intensity.

At Reynolds numbers of a few hundred thousand, a small (laminar) separation bubble usually forms on the suction side in the vicinity of the leading edge [5–8]. The size of this bubble depends on freestream turbulence intensity, making the maximal lift and drag coefficients sensitive to freestream conditions [5,6]. Nonetheless, the drag coefficient dependence on the angle of attack remains qualitatively the same (bucketlike) as at Reynolds numbers of a few million.

At Reynolds numbers of a few tens of thousands, the size of the separation bubble increases dramatically, and it usually bursts at a very small angle of attack. Indeed, conventional airfoils operating at these Reynolds numbers can produce steady lift only in a very limited range of angles of attack [9]. Moreover, most exhibit a drop in the drag coefficient once a certain angle of attack is exceeded (or, loosely speaking, they have a *double drag bucket* [2,3,10]). It is commonly accepted that the existence of the double bucket is associated with the laminar-to-turbulent transition occurring within the separation bubble [5,6], whereas the unsteadiness of the lift is associated with the wake instability developing right behind the trailing edge. Both phenomena are interrelated and hence need to be addressed en bloc. The laminar-to-turbulent transition process involving separation on the surface of an airfoil is the subject matter of this exposition.

Reynolds-averaged Navier–Stokes (RANS) simulations have only a limited ability to deal with separation-induced transition. Most commercial codes lack suitable models for the transition process and require the location in which the transition begins to be specified by the user. But this location is a priori unknown and it should be obtained as a part of the solution. Three-dimensional direct numerical simulations (DNS) can, in principle, deal with separation-induced transition [11], but they are time-expensive and, with 2006 computing capabilities, still impractical for parametric studies.

We propose that the main processes leading to separation-induced transition are essentially two-dimensional and therefore can be effectively analyzed using two-dimensional, and hence time-efficient, DNS. To demonstrate this, we undertook numerical and experimental study, combining flow visualizations with fully laminar, two-dimensional, time-accurate Navier–Stokes simulations over a fine mesh. The idea was to use flow visualizations for substantiating the 2-D assumption and validating the numerical simulations and to use numerical simulations for in-depth analysis of the flowfield.

The study involved a pair of conventional airfoils: the NACA-0009, a classical airfoil for Reynolds numbers of a few million, and the Eppler-61, a very successful airfoil for Reynolds numbers of a few hundred thousand. These particular airfoils were chosen because of their very different geometries (stemming from conceptually different designs) and because at a Reynolds number of a few tens of thousands, laminar-to-turbulent transition within separation bubble could be obtained for both of them [6]. The particular range of Reynolds numbers addressed in this study was 5000 to 60,000, which is relevant to mini and micro UAV development [12].

II. Methodology

A. Visualization

The water tunnel used for the present experiments was a vertical tunnel with a 45 by 45 by 100 cm test section, capable of continuous operation with test-section velocities between 1 and 40 cm/s. The

---

Presented as Paper 5311 at the 4th AIAA Theoretical Fluid Mechanics Conference, Toronto, 6–9 June 2005; received 10 January 2006; revision received 23 May 2007; accepted for publication 25 May 2007.

*Graduate Student, Faculty of Aerospace Engineering. Member AIAA.
†Visiting Professor, Faculty of Aerospace Engineering. Member AIAA.
‡Associate Professor, Faculty of Aerospace Engineering.

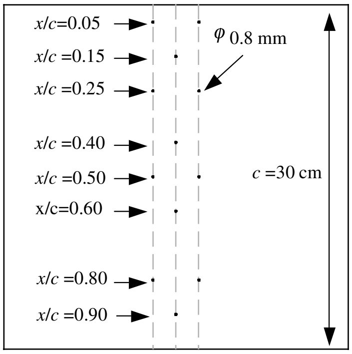

Fig. 1 Top view of a wing showing the dye-hole arrangement; each hole is 0.8 mm in diameter; leading edge is at the top.

pair of wings used (NACA-0009 and Eppler-61) had a chord of 30 cm and the same span; they were mounted between transparent end plates 25 cm across and 100 cm long (as long as the test section). Fourteen dye-injection holes, each 0.8 mm in diameter, were distributed on each side of a wing, between 5 and 90% chord locations, as shown in Fig. 1. The mechanical design is shown in Fig. 2. The dye was delivered to the injection holes through the side sting, which also functioned as a pivot for changing the wing's angle of attack.

Experimental uncertainties in the flow visualization experiments are associated mainly with the measurement of the wing angle of attack and the computation of the Reynolds number. The uncertainty in the angle of attack is estimated to be less than 0.5 deg. The uncertainty in the Reynolds number is composed of the uncertainty in the value of the pertinent kinematic viscosity (due to 0.5°C uncertainty in the water temperature) and of the uncertainty in the measured flow velocity (about 0.25 cm/s); it is listed in Table 1.

The main motivation for undertaking flow visualizations was to substantiate the 2-D flow assumption. Figure 3 depicts a top view of the NACA-0009 suction side at AOA ranging between 0 and 10 deg and a Reynolds number of 60,000. At a 0-deg AOA. the flow appears two-dimensional with no reversed-flow regions (Fig. 3a). As the AOA increases, the flow separates, but it is still two-dimensional in its nature (Figs. 3b–3d). The ordered two-dimensional structure of flow breaks at certain AOA, forming an essentially three-dimensional mixed flow (Figs. 3e and 3f). It is likely that fzat these conditions, the transition process has already begun. At yet higher AOA, a laminar separation bubble is formed with turbulent flow downstream of the bubbles' reattachment point (Figs. 3f–3h). A similar pattern can be observed with the Eppler-61 airfoil.

It is hoped that these observations are convincing enough to render 2-D assumption valid before the onset of the transition process. An unequivocal justification of 2-D assumption will, eventually, come from a good agreement between experimentally observed flow patterns and those simulated numerically based on 2-D assumption; these patterns will be discussed in the following sections and, in particular, in Sec. III.

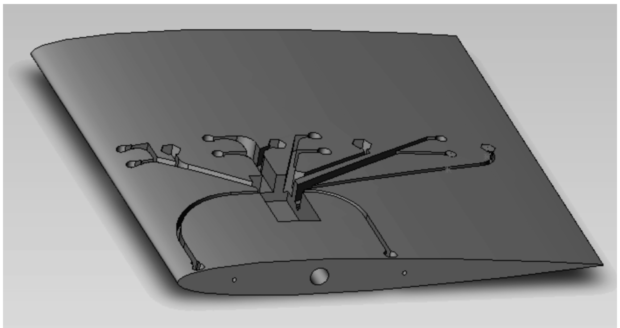

Fig. 2 Water-tunnel model of the NACA-0009 with the underskin arrangement for the dye holes.

Table 1 Reynolds number uncertainty

Reynolds number	5000	20,000	40,000	60,000
Uncertainty - %	20	9	7	6

B. Simulations

All numerical results presented in this paper were obtained running a time-accurate, two-dimensional, incompressible Navier–Stokes code using the method of artificial compressibility. The numerical scheme was implicit, first order in time, and second order in space. No turbulence model was incorporated in the code. To resolve the fine structures of the vortex shedding, fine meshes of 1596 by 90 cells with a C-topology were generated. There were 260 cells along the airfoil surface. Those cells were less than 10^{-2} chords long and 10^{-3} chords high; the height of the cells was less than the characteristic shear length $\nu\sqrt{\rho/\tau_w}$ at the highest Reynolds number solved. Several cases were simulated using both finer and coarser meshes; these are listed in Table 2. The computational domain extended from 20 chords upstream of the leading edge to 50 chords downstream of the trailing edge and 20 chords above and below the airfoil. Details of the computational meshes are shown in Fig. 4.

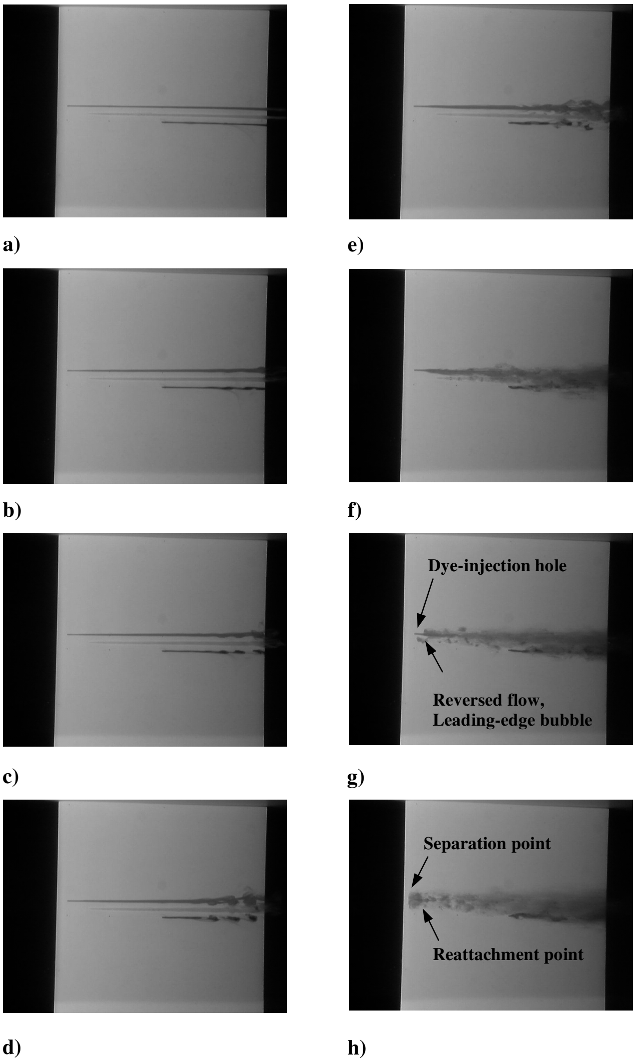

Fig. 3 Top view of the suction side of the NACA-0009 airfoil at $Re = 59,600$; AOA is increasing from 0 to 10 deg with an approximately 1-deg difference between pictures: a) 2-D attached flow; b) 2-D flow, separation point in the vicinity of the trailing edge; c–d) 2-D ordered vortex flow; e–f) breakdown into 3-D flow, 3-D onset point moves upstream; g–h) laminar bubble formation; turbulent flow can be observed downstream of the reattachment point.

Table 2 Meshes used

Mesh	Nominal	1	2	3	4	5	6
Longitudinal divisions (parts of 1596)	1	1/2	1	1/2	2	1	1
Lateral divisions (parts of 90)	1	1/2	1/2	1	1	2	4

The integration time step was on the order of 10^{-3} of the characteristic time c/u_∞. The tracking quantities of the time-dependent solutions were the integral aerodynamic coefficients. Each run was stopped either when the coefficients reached steady values or became periodic. In general, the convergence was achieved after approximately 10×10^3 to 20×10^3 time steps, which is the time required for the initial conditions to be carried downstream and "leave" the computational domain. At each time step, the convergence was reached after 20 to 30 cycles (subiterations).

Simulations were computed for Reynolds numbers of 5000, 10,000 20,000, 40,000, and 60,000 and several angles of attack, typically between 0.2 and 5 deg. The basic solution at each Reynolds number was obtained at a 0.2-deg AOA. After reaching a steady state or periodic solution at this angle, the AOA was increased, starting new solution with the previous flowfield as the initial condition. The ultimate outcome of each simulation was the vorticity field. In the figures, the vorticity is coded using a grayscale map, with black saturated at the absolute value of $10u_\infty/c$ and white marking zero.

Because this study involved a large number of numerical simulations, the choice of the nominal 1596 by 90 mesh was a certain compromise between accuracy and computational time. It was chosen as the coarsest mesh for which simulated vorticity patterns qualitatively matched the visual flow patterns photographed at the water tunnel at all conditions (see the next section). Quantitative test of the mesh selection involved several conditions, which are listed in Table 3. At each condition, the pressure C_p and friction C_f coefficients on the airfoil surface were compared with those computed on both finer and coarser meshes (Table 2).

At test condition 1, both coefficients were essentially identical for all computational meshes tested and hence are not presented here. At test conditions 2 and 4, the coefficients did not change appreciably with mesh refinement, but did change with mesh coarsening (Figs. 5 and 6). Sensitivity of the friction coefficient at the leading edge to the mesh size is obvious in view of high-velocity gradients at that region; they did not justify the use of a finer mesh. At test condition 3, the flowfield about the airfoil was unsteady. Consequently, minimum, maximum, and one-period-average values are shown for each coefficient (Fig. 7). Practical identity between the coefficients computed over the nominal mesh and the finer mesh 5 is apparent. Note, in particular, the location of the point of the zero-friction coefficient, which is identical with those of the nominal mesh and the finer mesh.

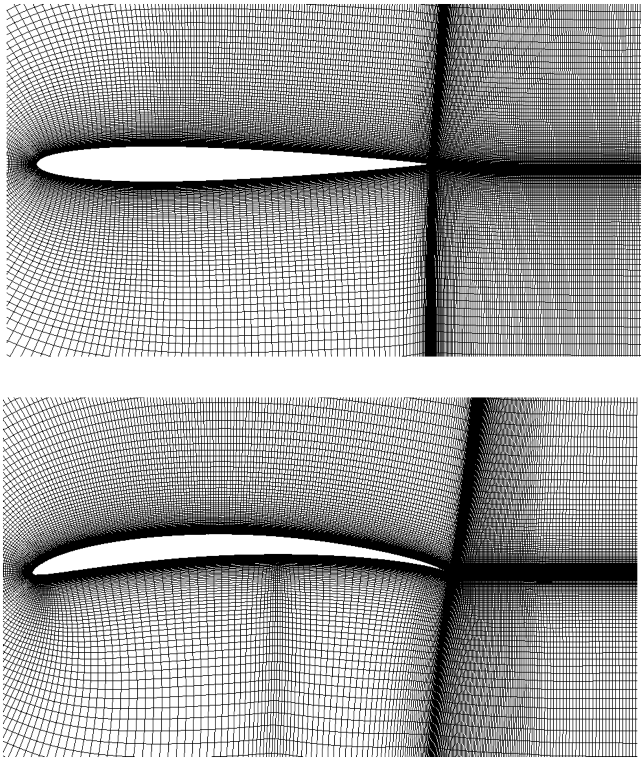

Fig. 4 Computational meshes for the NACA-0009 (upper) and Eppler-61 (lower) airfoils.

Table 3 Test conditions

Test condition	1	2	3	4
Reynolds number, thousands	10	20	20	60
AOA, deg	4	3	4	1.8

C. Comparison Between Simulations and Experiments

In general, very good agreement was obtained between visual flow patterns and simulated vorticity patterns for all cases considered, covering Reynolds numbers between 5000 and 60,000 and angles of attack between 0 and 5 deg. Because the boundary layer becomes thinner as the (chord-based) Reynolds number increases, the associated simulation accuracy may deteriorate if the grid geometry remains fixed. Hence, for a fixed grid, obtaining good agreement between simulations and visualizations at high Reynolds numbers is suggestive of comparably good agreement at lower Reynolds numbers. The following comparison was made at the higher range of the Reynolds numbers studied.

Two representative examples can be found in Figs. 8 and 9. In the first figure, the simulated vorticity field about the NACA-0009 at a Reynolds number of 60,000 and a 0.2-deg AOA is compared with the dye traces photographed at almost the same conditions; in the second figure, the comparison is repeated for the Eppler-61 at a Reynolds number of 40,000 and a 2-deg AOA. The similarity between the simulation and experiment is evident; in particular, the wavelength of the vortex shedding is practically identical, as is the general flow pattern in the vicinity of the airfoil's trailing edge, and so is the location of the separation point on the suction side of the Eppler-61 airfoil (shown by the dashed line). A small discrepancy in the AOA at which simulated patterns match those observed is attributed to the wing's mounting tolerance inside the water tunnel (0.5 deg).

With generally good agreement established between experimental and simulated flow patterns, the following discussion and analysis will be based on a free mix between the two.

III. Flowfields About NACA-0009 and Eppler-61 Airfoils

A. NACA-0009

At a Reynolds number of 5000, the flow appears locally stable up to a 5-deg AOA (Figs. 10a–10c). At that angle, the flow downstream of the airfoil becomes unstable and a periodic wake with one dominant wavelength (frequency) is formed; the flow around the airfoil remains practically steady (Fig. 10c).

At a Reynolds number of 10,000, the flow behaves qualitatively the same, with wake instability starting at a 3 deg instead of a 5-deg AOA (Fig. 11b). The onset of wake instability gets closer to the airfoil's trailing edge as the AOA increases, and at 5 deg, it begins in the near vicinity of the airfoil's trailing edge (Fig. 11c). No reattachment on the upper surface can be observed.

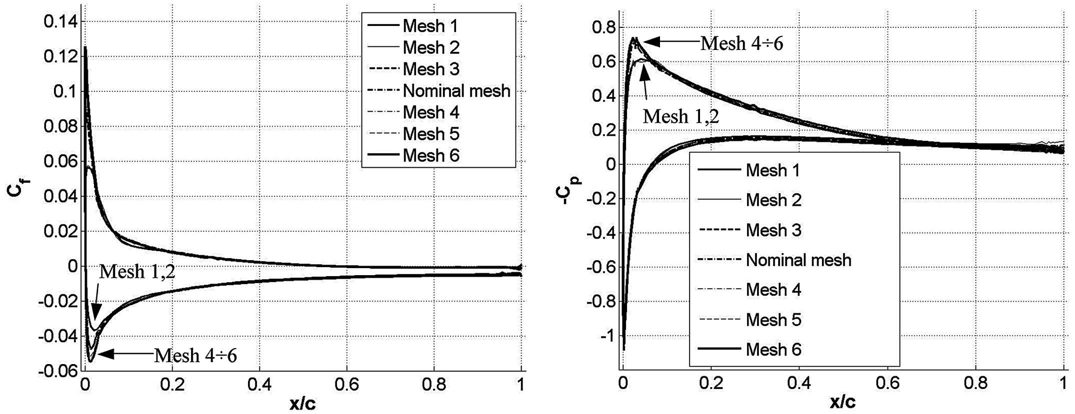

Fig. 5 Grid convergence checks for the NACA-0009 airfoil at $Re = 20,000$ and $AOA = 3\,\mathrm{deg}$; friction coefficient (left) and pressure coefficient (right).

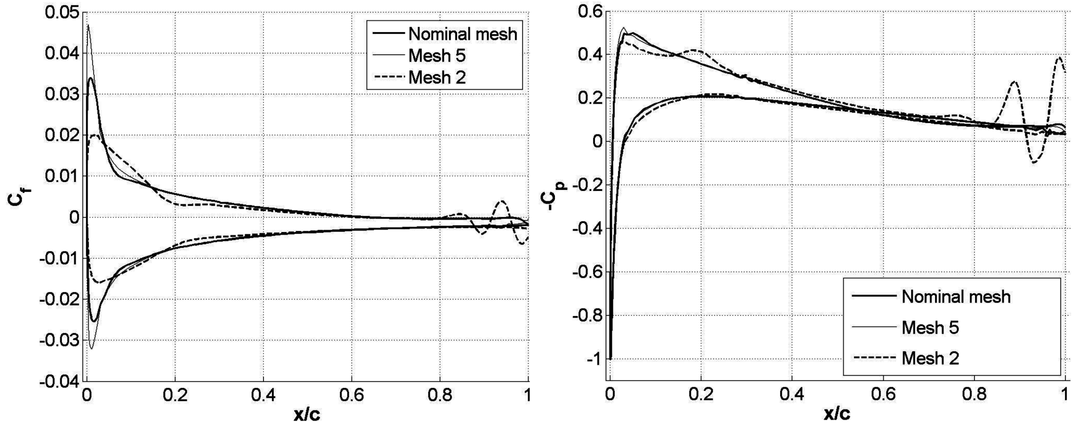

Fig. 6 Grid convergence checks for the NACA-0009 airfoil at $Re = 60,000$ and $AOA = 1.8\,\mathrm{deg}$; friction coefficient (left) and pressure coefficient (right).

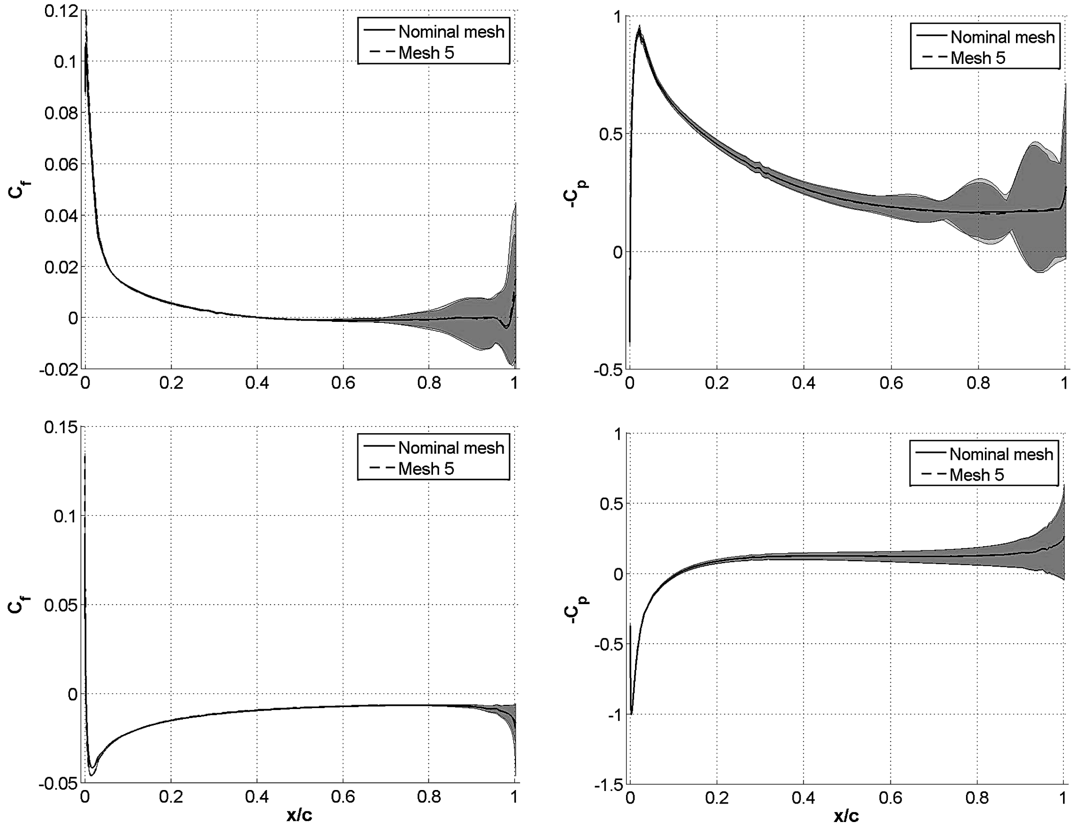

Fig. 7 Grid convergence checks for the NACA-0009 airfoil at $Re = 20,000$ and $AOA = 4\,\mathrm{deg}$; friction coefficient (left) and pressure coefficient (right); upper panels describe the pressure and friction coefficients distributions at the suction side of the airfoil, and the lower panel refer to the airfoil's pressure side; gray regions represent the maximal variation of the pressure and friction coefficients; continuous and broken lines are their time-averaged distributions over one period.

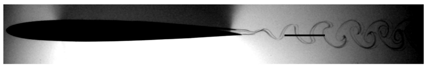

a) Water tunnel, *Re*=59,600 and AOA=0 deg

b) Simulation, *Re*=60,000 and AOA=0.2 deg

Fig. 8 Dye traces over the NACA-0009 in the water tunnel (top) and simulated vorticity field (bottom).

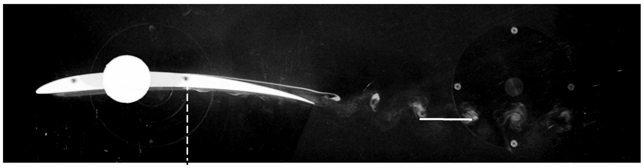

a) Water tunnel, *Re*=44,700 and AOA=2 deg

b) Simulation, *Re*=40,000 and AOA=2 deg

Fig. 9 Dye traces over the Eppler-61 in the water tunnel (top) and simulated vorticity field (bottom).

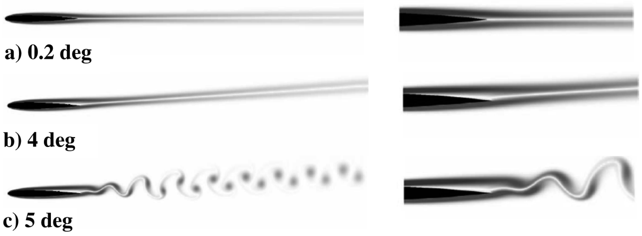

a) 0.2 deg

b) 4 deg

c) 5 deg

Fig. 10 Contours of equal vorticity at a Reynolds number of 5000 and various AOA; panels on the right are blowups of the respective panels on the left.

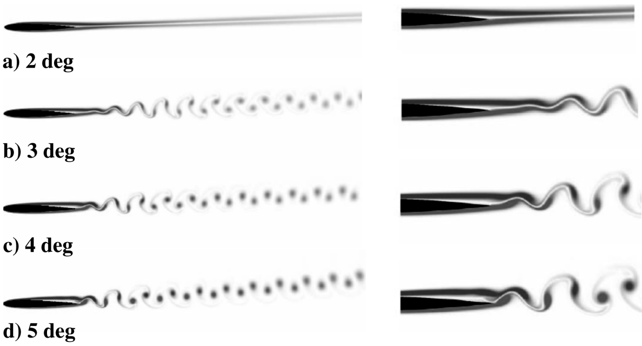

a) 2 deg

b) 3 deg

c) 4 deg

d) 5 deg

Fig. 11 Contours of equal vorticity at a Reynolds number of 10,000 and various AOA; panels on the right are blowups of the respective panels on the left.

At a Reynolds number of 20,000, the wake is unstable even at a 0.2-deg AOA (Fig. 12a); again, the onset of instability gets closer to the trailing edge as the AOA increases (Figs. 12b and 12c). At a 4-deg AOA, the Kelvin–Helmholtz instability [13] begins above the suction (upper) side of the airfoil and a new wavelength (frequency) appears in the flowfield (Fig. 12d). At a 4.5-deg AOA, a subharmony of the basic vortex shedding becomes dominant (Fig. 12e).

This pattern is confirmed by water-tunnel flow visualizations. At a 0-deg AOA, the flow is attached and the instability develops relatively far from the airfoil's trailing edge. The actual distance at which the instability becomes visible varies between the simulation and the experiment (Figs. 12a and 13a), probably because of the difference in the disturbances magnitude and the wing's mounting-

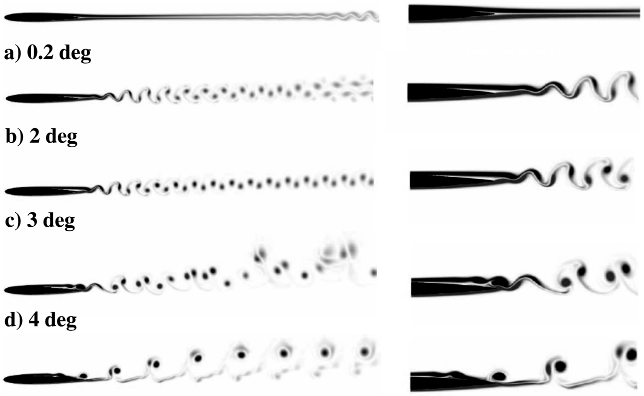

a) 0.2 deg

b) 2 deg

c) 3 deg

d) 4 deg

e) 4.5 deg

Fig. 12 Contours of equal vorticity at a Reynolds number of 20,000 and various AOA; panels on the right are blowups of the respective panels on the left.

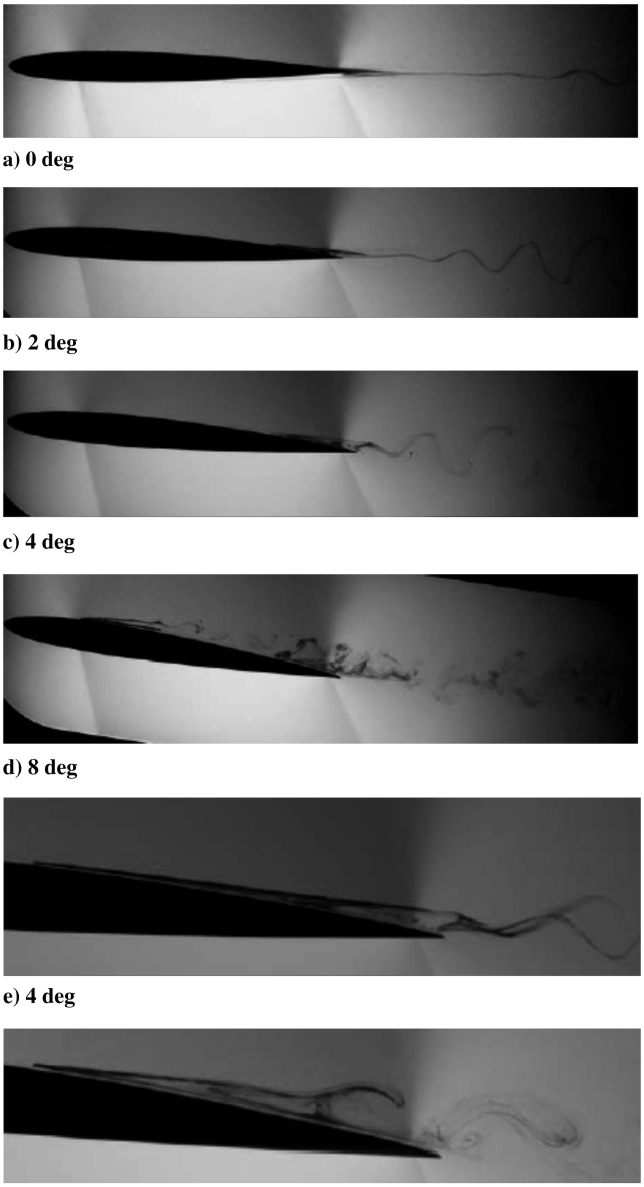

a) 0 deg

b) 2 deg

c) 4 deg

d) 8 deg

e) 4 deg

f) 6 deg

Fig. 13 Dye traces over the NACA-0009 at a Reynolds number of 19,360 and various AOA.

angle uncertainty. At an AOA of 2 deg, the simulation and the experiment agree on the instability onset, about a half-chord downstream of the airfoil's trailing edge (Figs. 12b and 13b). As the AOA increases, the natural vortex-shedding forms and separated flow regions become apparent at the suction side of the airfoil, in the vicinity of its trailing edge (Figs. 13b and 13c); a shallow laminar bubble can be seen at a 4-deg AOA (Figs. 13c and 13e). At a 6-deg AOA, the vortex-shedding process starts at the suction side of the airfoil (Fig. 13f) and it moves closer to the leading edge as the AOA increases. At an 8-deg AOA, the flowfield no longer appears to be laminar (Fig. 13d).

This pattern repeats itself at a Reynolds number of 40,000. As long as no reattachment occurs on the upper surface, the wake is ordered with a single dominant wavelength. As the flow reattaches on the upper surface (forming a separation bubble) the vortex shedding becomes unordered. At a 7-deg AOA, the flow is attached to the airfoil, the dye traces are mixed, and therefore the flow can be considered transitional/turbulent.

Simulated tangential velocity profiles are shown in Fig. 14. The light gray area marks the reversed-flow region; its boundary is the dividing streamline. The darker gray regions mark the maximal velocity fluctuation at each distance from the wing surface. Theoretical study of [14] implies that when maximal reversed-flow velocity exceeds 20% of the freestream velocity U_∞, the flow becomes globally unstable. Indeed, with small-amplitude reversed-flow velocity, the flow is stable at Reynolds numbers of 5000 and 10,000. At a Reynolds number of 20,000 and a 4-deg AOA with a time-averaged reversed-flow velocity of 11% and amplitude of 18% of the freestream velocity (i.e., maximal instantaneous reversed-flow velocity of about 30% of the freestream velocity), the flow seems to be marginally stable (Fig. 14b). At a 5-deg AOA, with a time-averaged reversed-flow velocity of 13% and amplitude of 40% of the freestream velocity, the laminar bubble reattaches and unsteady noncoherent vortices shed downstream (Fig. 14c). At a Reynolds number of 20,000, the separation point is sensitive to AOA and changes from 56% chord location at a 3-deg AOA to 10% chord at a 5-deg AOA. Although the boundary-layer profiles are steady at a 3-deg AOA, at a 4-deg AOA, the flow within the laminar bubble is unsteady with significant undulations, and at a 5-deg AOA, the bubble reattaches, forming an unsteady wake after the reattachment point. Qualitatively, the same phenomenon was also observed at higher Reynolds numbers. In general, as the Reynolds number increases, the separation starts earlier, mainly due to increased velocity gradients.

B. Eppler-61

In general, the basic flow pattern about this airfoil is similar to that about the NACA-0009. At low AOA, it has an ordered structure, characterized by a single wavelength; the wavelength decreases with increasing Reynolds number and remains independent of the AOA; at higher AOA, the single-wavelength ordered structure breaks up. In particular, however, there are a few differences. One difference is that the flow about the Eppler-61 remains laminar up to higher AOA. It seems that the laminar bubble on the suction surface of the Eppler-61 is retained at an almost-constant position, whereas that over the suction side of the NACA-0009 moves upstream as the AOA increases. Another difference is that the wake instability starts about the trailing edge of the Eppler-61 and keeps this position irrespective of the AOA; for the NACA-0009, it starts far downstream at low AOA and moves upstream with increasing AOA. It is plausible that this behavior of the Eppler-61 airfoil can be attributed to its curvature and hence to the pressure distribution along it. Two representative flow visualizations at Reynolds numbers of 5000 and 44,700 as functions of the AOA are presented in Fig. 15.

Computational results show similar trends. Indeed, at Reynolds numbers of 5000 and 10,000 and AOA between 1.4 and 5 deg, the natural vortex shedding has only one dominant frequency. Similar behavior of the flow in the vicinity of the airfoil's trailing edge is preserved up to a Reynolds number of 40,000, and more than one frequency appears above an AOA of 5 deg (Figs. 9b and 15).

IV. Discussion

The preceding observations suggest that at Reynolds numbers from 5000–60,000 and small AOA, the flow pattern about an airfoil evolves in three phases. In the first phase, the flow is steady, with no interaction between the upper- and lower-surface flows in the

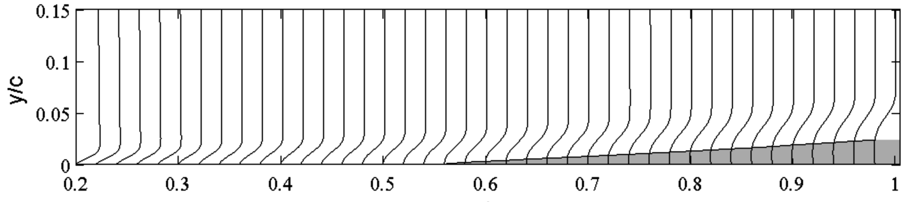

a) 3 deg

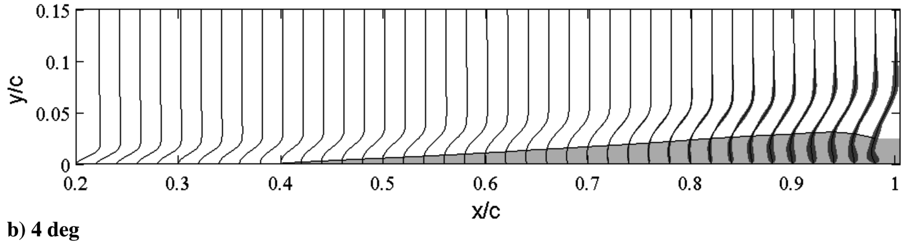

b) 4 deg

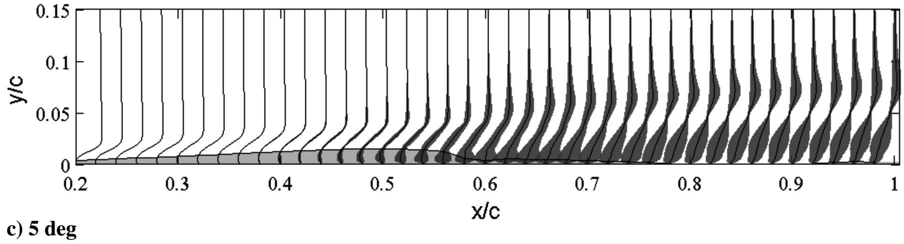

c) 5 deg

Fig. 14 Boundary-layer velocity profiles over the NACA-0009 at a Reynolds number of 20,000 and various AOA; light gray marks the separated flow region, black lines mark the local time-averaged velocity profiles, and dark gray regions about the respective time-averaged profiles mark all the instantaneous velocity profiles that comprise the average one.

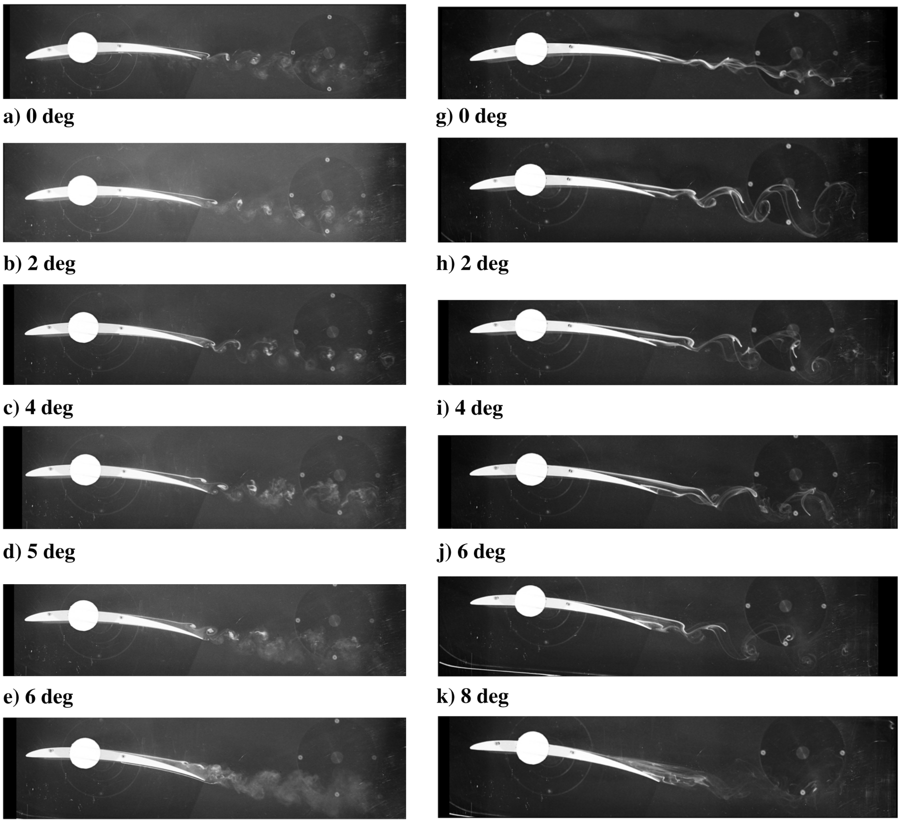

a) 0 deg **g) 0 deg**

b) 2 deg **h) 2 deg**

c) 4 deg **i) 4 deg**

d) 5 deg **j) 6 deg**

e) 6 deg **k) 8 deg**

f) 8 deg **l) 10 deg**

Fig. 15 Dye traces over the Eppler-61 airfoil at a Reynolds number of 5000 (left panels) and 44,700 (right panels) at various AOA.

vicinity of the airfoil. This phase was evident with the NACA-0009, but not with the Eppler-61. The existence of this phase depends on the basic (unperturbed) flowfield over the airfoil. If the flow has no large velocity gradients, as represented by the flow over the NACA-0009 at low AOA, the two vorticity sheets inferred by these velocity gradients could coexist without interaction. If the contrary is true (i.e., if the velocity gradients are large, as represented by the flow over the Eppler-61 at any AOA), the two vorticity sheets interact, forming an ordered vortex street.

In the second phase, the flow is dominated by a single wavelength with ordered concentrated vortices in the wake of the airfoil. Hydrodynamic stability analysis of a vortex street suggests that the most stable vortex arrangement for infinitesimal disturbances is when the ratio between lateral and longitudinal spacing of counter rotating vortices (vortex aspect) is 0.28 [15]. Indeed, the measured vortex aspect at the minimal AOA at which the vortex street could be observed was about 0.28 (Fig. 16).

In the third phase, flow disturbances appear and break up the ordered structure of the wake. The flow disturbances originate from the separated flow region that acts as a wide-bandwidth-noise generator. This noise induces large velocity variations and interacts with the least stable mode of the wake. According to [14], a vortex street is mostly unstable due to disturbances of the wavelength that is an integer multiple (a subharmony) of the original vortex street wavelength. A representative example is the NACA-0009 at a Reynolds number of 20,000. Up to a 3-deg AOA, the two vortex sheets interact downstream of the airfoil's trailing edge (Figs. 12a–12c). Although the entire flow is periodic, the flow about the airfoil is steady (Fig. 14a) At a 4-deg AOA, the ordered structure of the vortex street breaks up (Fig. 12d), and at a 4.5-deg AOA (Fig. 12e), it has two dominating wavelengths: the original vortex-shedding wavelength and its subharmony. In contrast with the steady flow about the airfoil and in the bubble at a 3-deg AOA, the flow in the bubble at a 4-deg AOA is unsteady.

These three phases are summarized in Fig. 17. The dark gray region in the figure marks those combinations of the angle of attack and the Reynolds numbers for which the wake is ordered in the immediate vicinity of the airfoil with no concentrated vortices (phase 1). The white region marks those combinations of the angle of attack and the Reynolds number for which the wake appeared as ordered vortex street dominated by a single wavelength (phase 2), and the light gray region denotes the conditions in which no order was observed in the wake (phase 3).

Experimental cases were color-coded, with squares denoting the experimental conditions in which no instability was observed in the vicinity of the trailing edge (phase 1), the diamonds denoting the cases were the ordered wake structure was ordered (phase 2), and the left-point triangles denoting those cases in which the wake was observed having no order (phase 3). Also marked in the figure (right-point triangles) are those cases in which the flow was mixed and attached; we believe that these cases can be associated with the second drag-bucket conditions.

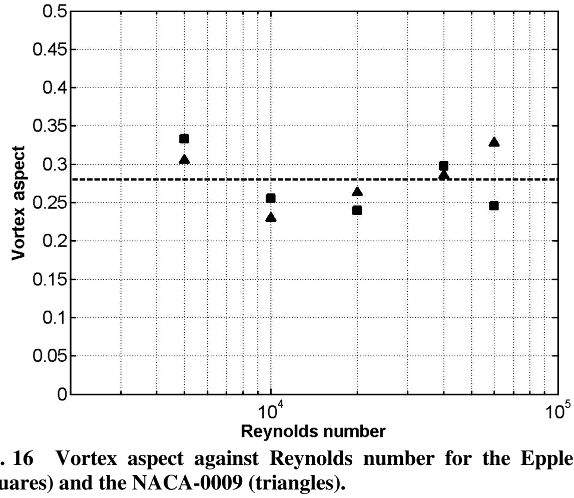

Fig. 16 Vortex aspect against Reynolds number for the Eppler-61 (squares) and the NACA-0009 (triangles).

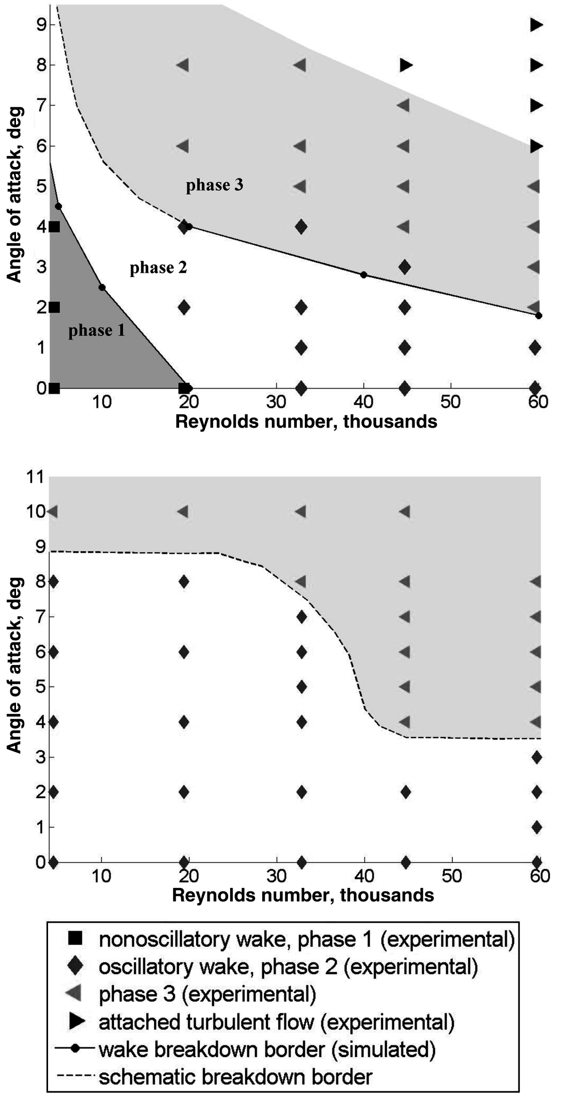

Fig. 17 Flowfield phase classification as a function of angle of attack and Reynolds number for the NACA-0009 (top) and Eppler-61 (bottom); computational results are bordered by the dashed line; some of the computational and experimental points can be found in the preceding figures.

Simulated borders between the phases of the NACA-0009 (marked by the solid lines on the top plate of Fig. 17) seem to accord with the experimental observations at all Reynolds numbers tested, including those above 20,000, which was set as our caution limit for quantitative analysis with numerical simulations.

Phase 1 conditions were not found for the Eppler-61 at any Reynolds number, for reasons already mentioned. For this airfoil, the AOA at which laminar separation occurs (marking the transition between phases 2 and 3) is practically independent of the Reynolds number, as long as it remained below 30,000; this AOA drops dramatically when 30,000 is exceeded.

V. Conclusions

This study addresses the first stages of the laminar-to-turbulent transition for NACA-0009 and Eppler-61 airfoils, with an emphasis on the two-dimensional flow mechanisms involved in the process. The study is based on a mix between high-fidelity, two-dimensional, laminar Navier–Stokes simulations and flow visualizations, with visualizations substantiating the assumptions underlying the simulations and with simulations providing in-depth details of the flowfield. We have not seen a comparable approach elsewhere.

The simulated boundary-layer velocity profiles suggest diminishing flow stability within the laminar bubble, which turns into a global instability when the reversed flow within the bubble becomes excessive, in complete agreement with results reported elsewhere. The good agreement between the simulated and observed flow patterns holds as long as the flow remains essentially two-dimensional.

The study shows that contrary to a local transition found in the laminar bubble at Reynolds numbers of a few hundred thousand, the transition process at Reynolds numbers of a few tens of thousands is no longer local. At these Reynolds numbers, the separation region interacts with the basic flowfield, which is unsteady and periodic in most cases.

Acknowledgments

This work was partially funded by the Israel Defense Directorate of Research and Development (DDR&D) under grant no. 397840. The help of B. E. Karlin with water-tunnel experiments is acknowledged.

References

[1] Kunz, P. J. and Kroo, I., "Analysis and Design of Airfoils for Use at Ultra-Low Reynolds Numbers,"*Fixed and Flapping Wing Aerodynamics for Micro Air Vehicle Application*, Progress in Astronautics and Aeronautics, Vol. 195, AIAA, Reston, VA, 2001, pp. 35–60.

[2] Jacobs, E. N. and Sherman, A., "Airfoil Section Characteristics as Affected by Variations of the Reynolds Number," NACA, Rept. 586, 1937.

[3] Selig, M. S., Lyon, C. A., Giguere, P., Ninham, C. P., and Guglielmo, J. J., *Summary of Low-Speed Airfoil Data: University of Illinois at Urbana–Champaign Low-Speed Airfoil Tests*, Vol. 2, SoarTech Publications, Virginia Beach, VA, 1996.

[4] Gault, D. E., "A Correlation of Low-Speed, Airfoil-Section Stalling Characteristics with Reynolds Number and Airfoil Geometry," NACA, TN 3963, Mar. 1957.

[5] O'Meara, M. M., and Mueller, T. J., "Laminar Separation Bubble Characteristics on an Airfoil at Low Reynolds Numbers," *AIAA Journal*, Vol. 25, No. 8, Aug. 1987, pp. 1033–1041.

[6] Mueller, T. J., and Burns, T. F., "Experimental Studies of the Eppler-61 Airfoil at Low Reynolds Numbers," AIAA Paper 82-0345, Jan. 1982.

[7] Cheng, H. K., and Smith, F. T., "The Influence of Airfoil Thickness and Reynolds Number on Separation," *Journal of Applied Mathematics and Physics*, Vol. 33, Mar. 1982, pp. 151–180.

[8] Tani, I., "Low-Speed Flows Involving Bubble Separations," *Progress in Aeronautical Sciences*, Vol. 5, Dec. 1964, pp. 70–103.

[9] Ghia, K. N., Osswald, G., and Ghia, U., "Study of Low-Reynolds Number Separated Flow Past the Wortmann FX 63-137 Airfoil,"*Low Reynolds Number Aerodynamics*, edited by T. J. Mueller, Lecture Notes in Engineering, Vol. 54, Springer–Verlag, Berlin, 1989, pp. 58–69.

[10] Grundy, T. M., Keefe, G. P., and Lowson, M. V., "Effects of Acoustic Disturbances on Low Re Aerofoil Flows,"*Fixed and Flapping Wing Aerodynamics for Micro Air Vehicle Application*, edited by T. J. Mueller, Progress in Astronautics and Aeronautics, Vol. 195, AIAA, Reston, VA, 2001, pp. 91–113.

[11] Maucher, U., Rist, U., Kloker, M., and Wagner, S., "DNS of Laminar-Turbulent Transition in Separation Bubbles," *High Performance Computing in Science and Engineering 99*, edited by E. Krause, and W. Jager, Springer–Verlag, Berlin, 2000, pp. 279–294.

[12] Mueller, T. J., and DeLaurier, J. D., "An Overview of Micro Air Vehicle Aerodynamics," *Fixed and Flapping Wing Aerodynamics for Micro Air Vehicle Application*, edited by T. J. Mueller, Progress in Astronautics and Aeronautics, Vol. 195, AIAA, Reston, VA, 2001, pp. 1–10.

[13] Drazin, P. G., and Reid, W. H., *Hydrodynamic Stability*, Cambridge Univ. Press, Cambridge, England, U.K, 1981, pp. 14–22.

[14] Rist, U., and Maucher, U., "Investigations of Time-Growing Instabilities in Laminar Separation Bubbles," *European Journal of Mechanics, B/Fluids*, Vol. 21, No. 5, 2002, pp. 495–509.

[15] Saffman, P. G., *Vortex Dynamics*, Cambridge Univ. Press, Cambridge, England, U.K., 1992, pp. 133–138.

R. So
Associate Editor